Focusing of light following a 4-f pulse shaper: considerations for quantum control

Sussman, Benjamin J.; Lausten, Rune; Stolow, Albert

Publisher's version / Version de l'éditeur:
https://doi.org/10.1103/PhysRevA.77.043416
Physical Review A, 77, 4, pp. 043416-1-043416-11, 2008-04-23

Focusing of light following a 4-*f* pulse shaper: Considerations for quantum control

Benjamin J. Sussman, Rune Lausten, and Albert Stolow
Molecular Photonics, Steacie Institute for Molecular Sciences, National Research Council of Canada, 100 Sussex Drive, Ottawa, ON, Canada K1A 0R6
(Received 2 November 2007; published 23 April 2008)

The focusing of coherent light, modified by a spatial light modulator (SLM) based 4-*f* pulse shaper, is discussed in the context of scalar diffraction theory. Diffractive effects (including space-time coupling) in SLMs may alter the size and shape of a subsequent laser focus. A numerical approach is used to investigate the effects of some common phase masks on the properties of the laser focus. The extreme case of an alternating phase mask is considered in some detail, as it clearly illustrates the effects of space-time coupling. The results are compared to a simple analytic model. The potential influence of SLM diffractive effects on multiphoton quantum control studies is discussed and some approaches to minimizing undesirable diffractive effects are suggested.

DOI: 10.1103/PhysRevA.77.043416 PACS number(s): 37.10.Jk

I. INTRODUCTION

Shaped optical pulses have found great utility in controlling the evolution of quantum systems [1–7], in performing spectroscopies [8], and in enhanced multiphoton microscopies [9]. The shaping of optical pulses is often (but not always [10]) based upon the use of spatial light modulators (SLM). Shapers work by spatially dispersing the colors comprising an ultrashort pulse, whereupon the phase and amplitude [1,11], and polarization [12,13] of each spectral component within the pulse can be individually articulated with an electronically programmable device. Upon recombination of the spectral components, an essentially arbitrary output pulse can be created. The theory for ultrafast optical Fourier processing is well developed [14,15]. These studies have demonstrated, however, that the optical processing is not a purely one-dimensional process where each spectral component is modified independent of its spatial position in the beam. This effect, known as space-time coupling, can have a dramatic effect on the focusing of shaped pulses. The principal issue is that the spectral content—and hence time evolution—at each point within the focused output beam is not the same. The modification of the focus has potential implications for multiphoton quantum control, pump-probe, and related experiments, the effects of which are the main interest of this paper. As well, programmable modification of the focus holds some interesting opportunities for shaping foci and their associated nonlinear point spread functions.

A common SLM based 4-*f* pulse shaper design is depicted in Fig. 1. A grating disperses the colors and, at the focal plane of a one-to-one telescope, an SLM [e.g., a liquid crystal display (LCD)] is used to apply a phase and or amplitude mask to the spatially dispersed spectrum. The origin of the space-time coupling lies in the finite size of the optical elements and laser beam focus [14,15,11,16]. When the input beam is dispersed by the first grating, an individual spectral component is reflected into a particular direction and, due to its finite spatial extent at the focus, this single spectral component may straddle more than one LCD pixel. The extent of the spatial dispersion is determined by the input beam size, the lens focal length, and the geometric factors of the grating. The last two lenses (L2 and L3) act as a type of image relay, effectively mapping the straddled pixels to the experimental focus. Figure 2 illustrates the implications of space-time coupling. Shown here is the special case of a pulse composed of only two colors (red and blue), both of which straddle pixels at the focus. A binary amplitude mask is applied, such that every second pixel has zero transmission. The two colors are then propagated through lens L2, the second grating, and then lens L3. As a result, the red and blue pulses are relay imaged to the focus of lens L3, where it can be seen that the two colors are not overlapping. This particular diffractive effect would have serious implications for interpreting any observable that depended on both colors

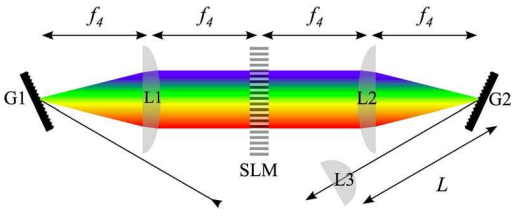

FIG. 1. (Color online) A typical spatial light modulator (SLM) based 4-*f* pulse shaper with optical components separated by a distance f_4. Following the SLM, the beam is propagated in free space a distance *L* and then focused by lens L3.

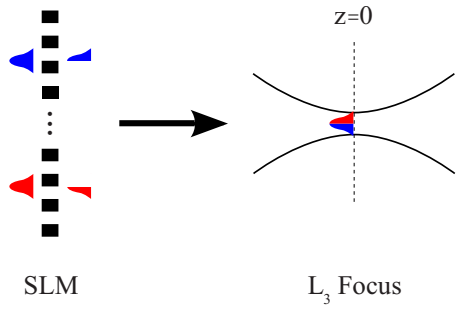

FIG. 2. (Color online) The origins of space-time coupling. Consider only two colors, red and blue, which are each focused onto the SLM of Fig. 1. The case where each color straddles two pixels of a binary amplitude mask is shown. The partially blocked colors are relay imaged to the focus of L3. It can be seen that the two colors do not overlap at the laser focus.

being absorbed by the sample. Although this example may be dramatic, it serves to show how diffractive effects due to SLMs can modify the spatial overlap (at a focus) of the different colors comprising the pulses. In fact, the space-time coupling due to SLMs has been previously discussed and applied in various situations. For example, a phase only mask has been used to achieve a combined phase and amplitude modulator [17] and phase only masks have been used to shape beam foci [18].

The paper is organized as follows. Section II details the origin of the space-time coupling and its related Appendix A derives the analytic result for the field at the experimental focal plane following lens L3. The second related Appendix B contains brief reviews of scalar diffraction theory and the Fresnel approximation. A number of numerical examples of diffraction situations are considered in Sec. III and compared with analytical results. Although extreme, the case of an alternating phase mask is considered in some detail to unambiguously illustrate the effects of space-time coupling at a subsequent laser focus and to develop "rules of thumb" for minimizing these effects in a given arrangement. Other types of masks and their effects on space-time coupling are also considered. In Sec. IV, in order to measure the potential implications of space-time coupling for multiphoton experiments, the propagation of the shaped pulse through the focal plane is considered. To quantify these effects on multiphoton branching ratios, we calculate and compare the spatial overlap integrals of different colors comprising the pulse, as well as volume integrated multiphoton transitions probabilities for different phase masks. Opportunities for shaping foci and some suggestions for minimizing undesired diffractive effects are discussed in the conclusion. For convenience, the notation used throughout is summarized in Table I.

TABLE I. Abridged notation summary. The appended numerical values are those used in the examples.

Variable or function	Definition
$e(x,z,t)$	Analytic electric field: $e(x,z,t)=E(x,z,t)e^{-2\pi i(f_z z-f_0 t)}$
$E(x,z,t)$	Analytic electric field pulse envelope: $E(x,z_0,t)=e^{-t^2/\tau_t^2-x^2/\tau_x^2}$
τ_t,τ_x	e^{-2} intensity half-width: $\tau_t=36$ fs, $\tau_x=1$ mm
τ_x'	Spatial envelope width at experimental focus: $\tau_x'=f_L\lambda_0/\pi\tau_x$
$a^x(f_x)$	Spatial Fourier transform of $a(x)$: $a^x(f_x)\equiv\int_{-\infty}^{\infty}a(x)e^{2\pi i f_x x}dx$
$a^t(f_t)$	Temporal Fourier transform of $a(t)$: $a^t(f_t)=\int_{-\infty}^{\infty}a(t)e^{-2\pi i f_t t}dt$
$\mathcal{F},\mathcal{F}^{-1}$	Fast Fourier and its inverse
f_x	Spatial frequency
f_t	Temporal frequency
f_0,λ_0	Central optical frequency and wavelength: 0.3747 fs^{-1}, 800 nm
L	Distance from SLM output to lens L3: 0 or 2 m
f_4	Focal length of lens in SLM: 15 cm
f_L	Focal length of lens following SLM: 6 cm
m_n	Transfer mask on pixel: $\{n\|1,2,3,\ldots,128\}$
W_p	Pixel width, 100 μm, for examples
β	Grating parameter $\beta=\cos(\theta_{\text{in}})/\cos(\theta_{\text{out}})$
γ	Grating parameter $\gamma=1/\cos(\theta_{\text{out}})f_0 d$
d	Grating line spacing: 1/600 mm
$\theta_{\text{in}},\theta_{\text{out}}$	Grating input and output angles: –0.2618, 0.8313, cf. [16]
ϕ	Transverse position on SLM, as a phase: $\phi=\lambda_0 f_4\gamma\pi/W_p f_t$

II. SPACE-TIME COUPLING

The evolution of an ultrafast laser pulse through the SLM based 4-f pulse shaper depicted in Fig. 1 can be understood in terms of Fresnel optics (see Appendix A). By propagating the pulse through each optical element (see Appendix B) the focal field at the experimental focus can be derived in terms of the input field space and time Fourier transform E_{in}^{xt} and the spatial mask (LCD) transfer function m,

$$E_{\text{focus}}^{t}(x,f_t)=E_{\text{in}}^{xt}\left(-\frac{x}{f_L\lambda_0},f_t\right)m\left(-\lambda_0 f_4\gamma f_t-\beta\frac{f_4}{f_L}x\right)e^{-i\pi L/\lambda_0 f_L^2 x^2}. \tag{1}$$

The superscripts x and t indicate a spatial or temporal Fourier transform, respectively. The argument of m indicates that the transverse position x at the experimental focus and the optical frequency f_t are linearly related to the transverse position on the mask

$$x_{\text{mask}}=-\lambda_0 f_4\gamma f_t-\beta\frac{f_4}{f_L}x. \tag{2}$$

If the process was one dimensional, each spectral element f_t would be associated with a single pixel or pixel position (x_{mask}). However, the finite spatial size effects introduce an additional dimension requiring the introduction of the the second term $\beta\frac{f_4}{f_L}x$, implying that a single color cannot be associated with a single pixel. Depending on the nature of the mask, this can introduce significant diffractive effects. At the focal plane of the pulse shaper, where the SLM is located, the lines of constant mask displacement (i.e., fixed pixel number) are denoted by $f_t+x\frac{\beta}{\gamma\lambda_0 f_L}=\text{const}$. As the frequency is changed, so is the associated pixel. Additionally, as the transverse focal position changes so does the associated pixel.

The origin of (1) can also be understood in terms of ray tracing. Due to its finite duration, an input beam is composed of many optical frequencies $f_t=c/\lambda$. Likewise, due to its finite spatial size, it is also composed of many spatial frequencies f_x. Each spatial frequency corresponds to a different input angle $\theta_{\text{in}}\approx\tan(\theta_{\text{in}})=cf_x/f_t=\lambda f_x$. The grating equation,

$$\sin(\theta_{\text{in}})+\sin(\theta_{\text{out}})=\frac{m\lambda}{d}, \tag{3}$$

therefore implies that each input spatial frequency (or input angle) and color will be dispersed to a particular angle θ_{out}

and pixel on the mask. The origin of the space-time coupling is that the output angle, and hence pixel, depends not only on the wavelength, but also on the input angle (which is varied due to the finite beam size).

III. EXPERIMENTAL FOCUS ISSUES

A. Periodic phase masks

To emphasize the effects of space-time coupling, the case of an alternating phase mask is considered. The extension to other phase masks is discussed in the following sections. A great deal of the experimental focal volume structure can be understood by noting that the SLM produces an effective grating at the focal plane, as illustrated by Fig. 2. The effective grating is a scaled mapping of the SLM mask to the experimental focal plane. The mapping is noted in (1), which gives the relationship between x (the transverse position at the L3) and x_{mask} (the transverse position at the SLM). At distances far from the plane, the structure can be explained in terms of the grating equation whereas in the near field, the structure depends strongly on the transverse position of the SLM, as will be shown. Note that x in the figures of this section represents the transverse direction at the L3 focus and due to geometric factors, like the relative focal lengths and grating parameters, a pixel width of 100 μm is mapped to 28 μm.

According to (1), at the experimental focus, each spectral component of $E^{t}_{\text{focus}}(x,f_t)$ is given by the input field Fourier transform multiplied by a scaled version of the LCD mask. The different spectral components are modified by a mask that is displaced depending on optical frequency and spatial position. For experiments where narrow linewidth excitations are important, the spatial variation of the mask at the focus is the main experimental concern, since the other frequencies are not utilized. (However, for multiphoton experiments, discussed below, the spatial overlap throughout the focus of two different narrow bandwidth components can be significantly altered by diffractive effects.) Therefore, some general features of a periodic phase mask can be understood by analytically considering a monochromatic Gaussian beam incident upon various spatial masks. In particular, periodic phase masks are typically used for creating time delayed pulse replicas. Consider the case where the transfer mask m_n on each pixel $\{n|n=1,2,\ldots,128\}$ alternates by a phase shift of π,

$$m_n = e^{i\pi \bmod(n,2)} = [1,-1,1,-1,\ldots]. \tag{4}$$

The time delay between pulses is created by the periodic modulation of the optical spectrum. The spatial period of the modulations is $2W_p$ which, via the first term on the right-hand side of (2), corresponds to optical spectrum variations with a period of $2W_p/\lambda_0 f_4 \gamma$. Hence the time spacing of the pulses is given by 2 times the inverse of that spacing $\lambda_0 f_4 \gamma / W_p = 2.85$ ps (see Table I for parameter values).

As a first step in discussing an alternating SLM phase mask analytically, consider an exponential phase mask $m(x)=\exp(-i\frac{2\pi}{2W_p}x)$. At the experimental L3 focus where $z=0$, the electric field is given by

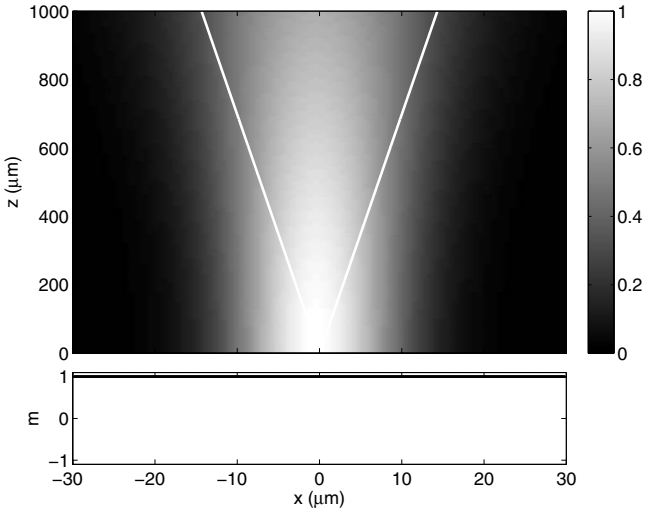

FIG. 3. The spatial intensity distribution at the focus of L3 of a Gaussian beam in the absence of a mask. In order to compare with subsequent figures, the first-order grating caustics are shown in white. The lower plot shows the mask function, m, applied to the SLM. Positive values correspond to a phase of 0, while negative correspond to a phase of π.

$$E(x,0,t) = e^{-x^2/\tau_x'^2} e^{-i2\pi/2W_p x_{\text{mask}}}. \tag{5}$$

The argument of the exponential can be rewritten, via (2), as

$$E(x,0,t) = e^{-x^2/\tau_x'^2} e^{i(2\pi x/T+\phi)}, \tag{6}$$

where the spatial period is given as $T=\frac{2W_p}{\beta}\frac{f_L}{f_4}$ and since the current concern is monochromatic beams, the frequency dependent part has been absorbed into a phase that represents a transverse translation across a pixel

$$\phi = \lambda_0 f_4 \gamma \frac{\pi}{W_p} f_t. \tag{7}$$

The phase corresponds to either a change in optical frequency or a physical transverse translation of the SLM, not an optical phase

The pulse may be analytically propagated using (A9) to obtain

$$E(x,z,t) = \frac{1}{\sqrt{q}} e^{-x^2/\tau_x'^2 q - i\pi(x_1-2x)/Tq+i\phi}, \tag{8}$$

where we have defined

$$x_1 = \frac{\lambda z}{T} \tag{9}$$

and

$$q(z) = 1 + i\frac{z}{z_R}, \tag{10}$$

where $z_R=\pi\tau_x'^2/\lambda$ is the Rayleigh range.

The corresponding intensity is given by (see Fig. 3).

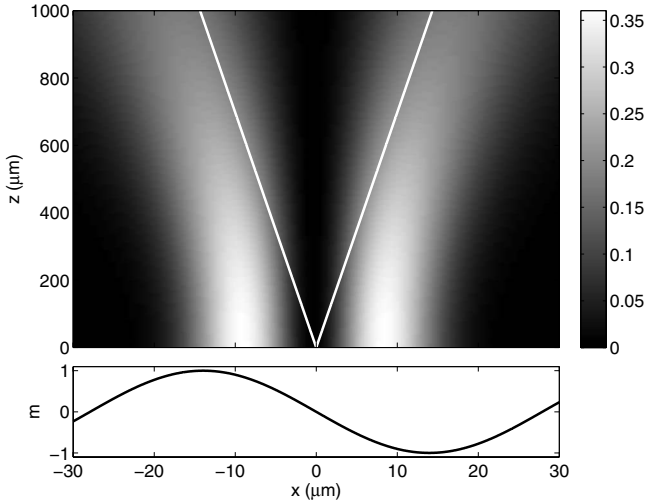

FIG. 4. The spatial intensity distribution at the focus of L3 following propagation through an SLM having a sinusoidal phase mask. The first-order grating caustics are shown in white. As discussed in the text, the sinusoidal mask can be considered as the lowest order Fourier expansion term of a square wave phase mask pattern.

$$I(x,z) = \frac{1}{|q|} e^{-2(x-x_1)^2/|q|^2\tau_x'^2}. \tag{11}$$

The incident beam is diffracted, as if it traversed a grating. The parameter x_1 is motivated from the transverse displacement of a beam following normal incidence on a grating, the geometry of which is given by (3) with the grating spacing $d=T$, and the distance from the grating of z:

$$x_k \approx z \tan(\theta_{\text{out}}) \approx z\frac{k\lambda}{T}. \tag{12}$$

The result (11) for an exponential phase mask can be extended to an alternating phase mask. An alternating phase mask with $m_{2j+1}=1$, $m_{2j}=-1$ and period T can be written as a sum of sinusoids,

$$m(x) = \frac{4}{\pi}\sum_{n=0}^{\infty} \frac{\sin\left((2n+1)\dfrac{2\pi x}{T}\right)}{2n+1}. \tag{13}$$

As an approximation we consider only the first term,

$$E(x,z=0) = e^{-x^2/\tau_x^2}\sin\left(\frac{2\pi x}{T}+\phi\right). \tag{14}$$

The pulse may be analytically propagated using (8) and its complex conjugate or (A9) directly to obtain

$$E(x,z) = \frac{1}{2i\sqrt{q}}(e^{-x^2/\tau_x'^2 q - i\pi(x_1-2x)/Tq+i\phi} - e^{-x^2/\tau_x'^2 q - i\pi(x_1+2x)/Tq-i\phi}). \tag{15}$$

The corresponding intensity is given by

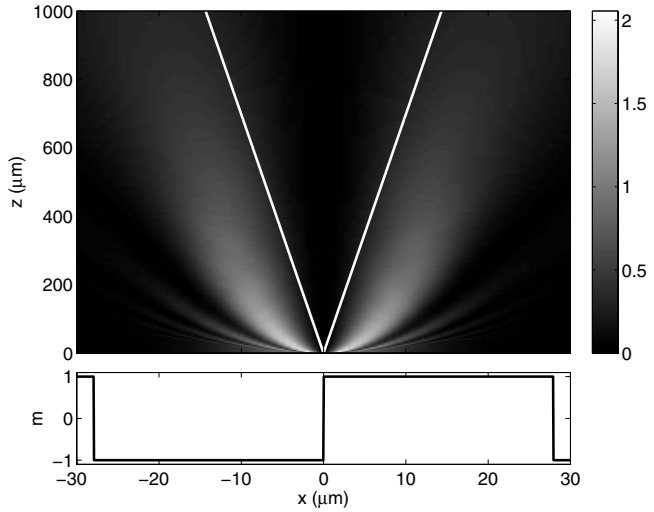

FIG. 5. The spatial intensity distribution at the focus of L3 following propagation through an SLM having a square wave phase mask. The first-order grating caustics are shown in white. The higher order caustics appear as bands that progress outwards. Note that x represents the transverse direction at the L3 focus, and due to geometric factors such as the relative focal lengths and grating parameters, a pixel width of 100 μm is mapped to 28 μm.

$$I(x,z) = \frac{1}{4|q|}\left\{ e^{-2(x-x_1)^2/|q|^2\tau_x'^2} + e^{-2(x+x_1)^2/|q|^2\tau_x'^2} + e^{-2(x^2+x_1^2)/|q|^2\tau_x'^2}\left[4\sin^2\left(\frac{2\pi x}{|q|^2 T}+\phi\right)-2\right]\right\}. \tag{16}$$

At large distances z, the first two terms in (16) dominate and beam caustics follow peaks at $\pm x_1$ corresponding to the first-order transmissions of a grating $k=\pm 1$ (Fig. 4): The alternating SLM mask is equivalent to placing a scaled transmission grating at the experimental focus. Within Fresnel limits, the hard edges of a true pixel would be represented by adding a sum of higher frequency sinusoid terms to (14). The higher frequency terms will diffract to higher order grating modes, and display banding (Fig. 5).

At closer distances z, the third term of (16) dominates. In this close regime, the structure and phase of the grating overshadows the ray interpretation of conventional grating orders observed at larger z. The caustics begin at the peaks of the sinusoid and move toward the asymptotes given by $\pm x_1$. As the grating size becomes smaller (which is equivalent to longer wavelength, smaller SLM pixels, longer f_4, or smaller input beam size), the incident beam fills more grooves of the effective grating and the field displays multislit interference. This results in a very complicated structure close to the focus (Fig. 6).

A transverse translation of the mask in the Fourier plane is equivalent to a change in phase of the mask ϕ. For example, for a ray to be deflected one-fourth of a pixel (i.e., a phase shift of $\phi=\pi/4$) the corresponding change in optical frequency would be $f_t=8.77\times10^{-5}$ fs^{-1}, or a wavelength shift of 0.187 nm. Therefore, for well dispersed pulses, small

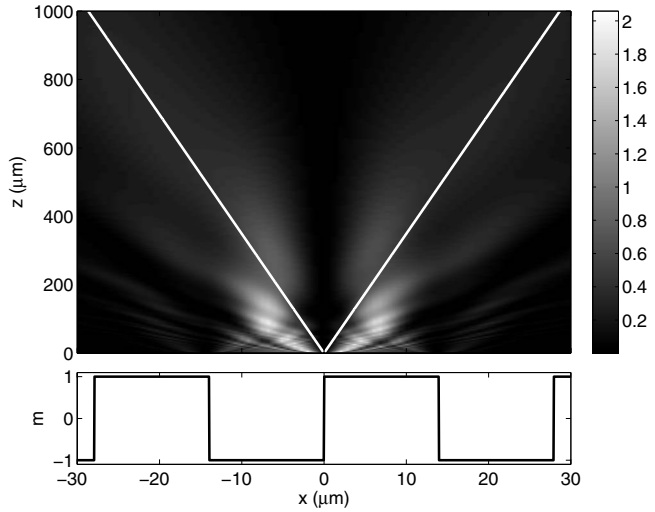

FIG. 6. The spatial intensity distribution at the focus of L3 following propagation through an SLM having a square wave mask with pixel size one-half that of Fig. 5. Equivalently, similar effects will occur at longer wavelengths. The first-order grating caustics are shown in white. The higher order caustics appear as bands that progress outwards. The intricate structure is caused by the increase from approximately two slits to four slits.

changes in frequency are equivalent to large pixel shifts on the mask. This is illustrated in Fig. 7 for a sinusoidal mask and in Fig. 8 for a square mask, which is a more accurate representation of an SLM.

These results demonstrate the nature of the space-time effects for particular frequencies. For ultrashort broad bandwidth pulses, the superposition of frequencies results in different temporal pulse shapes at different transverse positions.

B. Beam relaying

Propagation of an optical beam in free space causes a quadratic advancement of the phase front via (A9) As a result, a beam that is shaped and propagated a distance L before being focused by L3 may not have highest intensity at the focal plane [16].

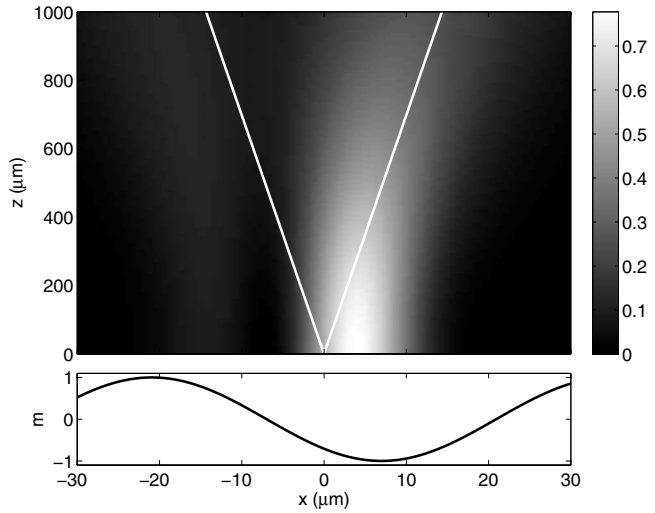

FIG. 7. The spatial intensity distribution at the focus of L3 following propagation through an SLM having a sinusoidal phase mask that has been translated by $\phi=\pi/4$. The first-order grating caustics are shown in white.

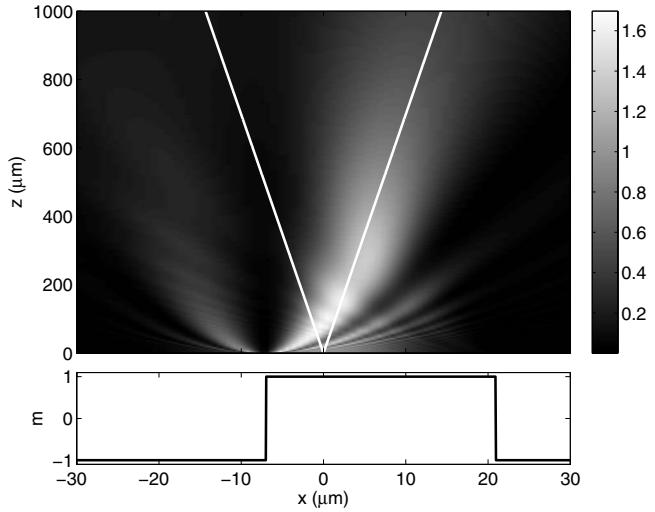

FIG. 8. The spatial intensity distribution at the focus of L3 following propagation through an SLM having a square wave phase mask that has been translated by $\phi=\pi/4$. The first-order grating caustics are shown in white. The higher order caustics appear as bands that progress outwards.

A Gaussian beam propagating in free space evolves according to (8), with $\phi=0$ and $T\to\infty$. Rationalizing the exponent as

$$E(z)=\frac{1}{\sqrt{q}}e^{-x^2/\tau_x^2|q|^2[1+(1-q)]} \tag{17}$$

indicates that the phase-front advance is given by the quadratic form $[q(z)-1]x^2/|q|^2\tau_x^2$. Similarly, the effect of a thin lens of focal length f_L is to introduce a quadratic phase,

$$e^{-\pi i f/cf_L x^2}. \tag{18}$$

Therefore, the combination of field-free propagation and a thin lens has the equivalent effect of changing the focal length to an effective focal length,

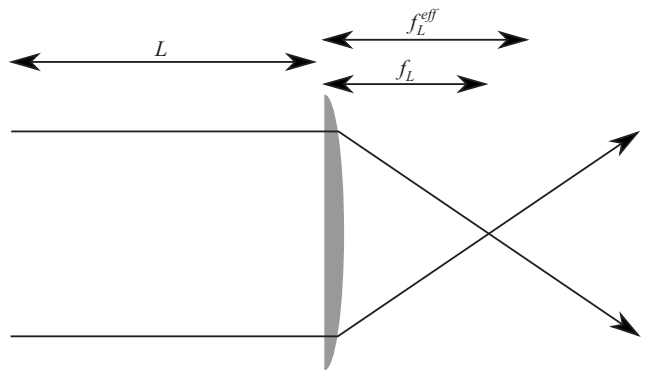

FIG. 9. Two transversely separated rays cross at the focus f_L. However, due to advancement of the phase front during propagation over distance L, the maximum peak intensity of each ray occurs where the phase front is flat, at f_L^{eff}.

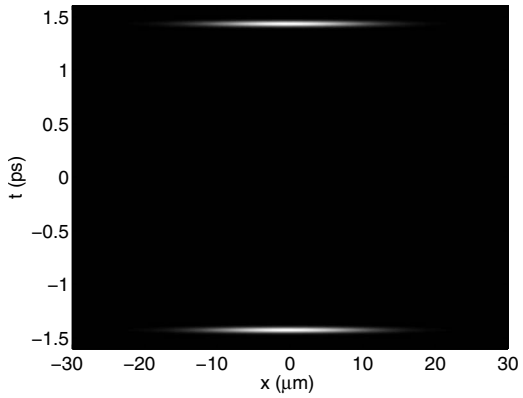

FIG. 10. The intensity profile at the focus following free space propagation through a distance $L=2$ m. The pulse replicas pass through the same transverse position at $x=0$, however, their intensity is higher at the effective focus (Fig. 11).

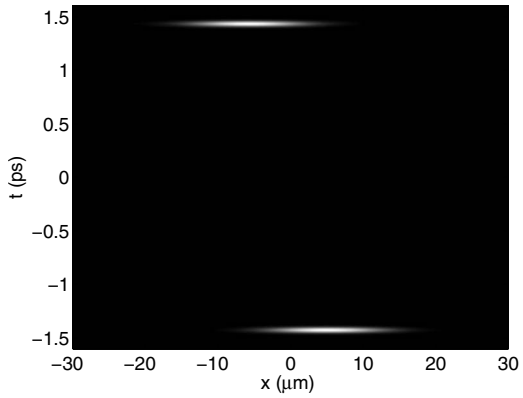

FIG. 11. The intensity profile at the effective focus f_L^{eff} following free space propagation through a distance $L=2$ m. Note that while the pulse replicas do not pass through the same transverse position, they are more localized than at the focus (Fig. 10) and hence the intensity is higher.

$$\frac{1}{f_L^{\text{eff}}} = \frac{1}{f_L} - \frac{\lambda\ \text{Im}[q(L)]}{\pi\tau_x^2|q|^2}. \tag{19}$$

Thus, the effect of propagation is to delay, beyond the focal plane, the point where the phase front is flat (Fig. 9).

For example, if an alternating phase mask is applied, pulse replicas with a transverse separation (due to space-time coupling) will be created. For pulses that propagated for $L=2$ m before reaching lens L3, the effective focal length is $f_L^{\text{eff}}-f_L=373$ μm beyond the focal length f_L. Due to the space-time coupling, the two pulse replicas are transversally offset in space and propagate toward the focus at opposite angles, crossing at the focus (Fig. 5). Pulse replicas that cross at the focus (Fig. 10) do not reach their smallest size until the effective focus (Fig. 11). As a result, experiments using pulses with significant space-time coupling will have complicated foci. This will result in complications for multibeam experiments, particularly pump-probe experiments. In order to avoid these propagation effects, optical image relaying of the G2 grating output can be used for $4f$-shaped pulses.

C. Pixelation-propagation effects

For a particular optical frequency, gratings behave, up to a geometric scaling factor β, essentially as a mirror. Grating G1 (Fig. 1) reflects an input optical frequency and L1 focuses it onto the LCD mask. Due to finite beam sizes, and regardless of experimental geometry, there will always be certain optical frequencies that straddle at least two pixels of the mask after focusing by L1. Since G2 also behaves like a mirror, lens L2 and L3 in combination act as an image relay of the mask focus: The spatial variation of the mask is mapped to the experimental focus. The discreetness of pixel steps means that there will be abrupt transverse variations in the phase at the L3 focus. As a result of the pixelation, there will be interference as the beam propagates. The pixelation at the focal plane is demonstrated in Fig. 12. It should be noted that the interference is due, not to the pixelation alone, but the spatial variation. The pixelation only serves to introduce high frequency components into the interference structure.

At the experimental focal plane of L3, the electric field has discrete steps in the transverse direction. Each step corresponds to an SLM pixel that has been relayed to the focal plane. For example, let the central step represent the field relayed from the central pixel. It is a function that is finite in the range $x=[0, W_p\frac{f_L}{\beta f_4})$ and zero elsewhere. Let the field from this pixel be represented by the product of a modulus and phase, $A(x,0)e^{ia(x,0)}$. As this light propagates in z, it evolves to $A(x,z)e^{ia(x,z)}$. Another contribution from a neighboring pixel which includes a phase shift ψ, is nonzero only in the range $x=[-W_p\frac{f_L}{\beta f_4}, 0)$ and is given by $B(x,z)e^{ib(x,z)}e^{i\psi}$. The total field is then given by

$$E(x,z) = A(x,z)e^{ia(x,z)} + B(x,z)e^{ib(x,z)}e^{i\psi} \tag{20}$$

and the intensity is given by

$$I(x,z) = A^2 + B^2 + 2AB\ \cos(b-a+\psi). \tag{21}$$

The cross term represents the propagation interference and its deviation from the case where $\psi=0$ is a measure of the influence of the pixelized phase shift. To consider the interference, the cross term is rewritten using a trigonometric identity,

$$2AB[\cos(b-a)\cos(\psi) + \sin(b-a)\sin(\psi)]. \tag{22}$$

The first term is proportional to $\cos(\psi)$ and represents the modification of the original interference that would be present when $\psi=0$. The second term (which vanishes for $\psi=0$) represents a new interference structure not present in the case when there is no phase shift. In order to minimize the interference structures in the focal volume, both terms should be small compared to the no phase shift case, which is to say it is usually sufficient for the second term to be small,

$$\psi \ll 1. \tag{23}$$

As discussed below more generally, nonresonant multiphoton transition probabilities (27) depend on the nth power of the electric field. Consider only the fastest changing terms of E^n,

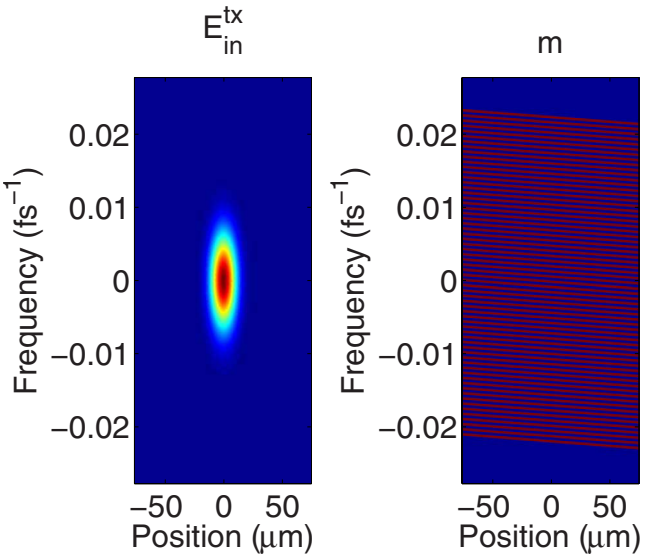

FIG. 12. (Color online) A graphical representation of the origin of space-time coupling at the focus, as given by (1) for the case when there is no free space propagation ($L=0$). The spatial structure of a pulse focused by L3 will be the product of these two figures. (Left-hand side) The spectral-spatial intensity of the focused input pulse $E^{xt}_{\text{in}}(-\frac{x}{f_4\lambda_0}, f_t)$. (Right-hand side) The alternating mask $m(-\lambda_0 f_4 \gamma f_t - \beta\frac{f_4}{f_L}x)$. The space-time coupling causes the pixel lines to tilt in frequency, contradicting the expectation that each spectral element in the pulse can be individually addressed by a single pixel.

$$E^n(\phi) \sim A^n e^{ina} + B^n e^{inb} e^{in\psi}. \tag{24}$$

In this case, the second cross term of the intensity is proportional to $\sin(n\psi)$. Therefore, in order to minimize pixelation-propagation effects, it is sufficient to require that the phase shifts between pixels, m_j and m_k satisfy (modulo 2π),

$$|\psi| = |\arg(m_j) - \arg(m_k)| \ll \frac{1}{n}. \tag{25}$$

Typically m_j and m_k are neighboring pixels. However, if the focal spot size on the LCD is large and covers numerous pixels, then m_j and m_k must include all pixels that the beam (for a particular color) illuminates.

IV. IMPLICATIONS FOR MULTIPHOTON EXPERIMENTS

The interference between multiphoton processes lies at the heart of coherent control methods. Controlling the phase of different pathways to a final state provides a means of producing constructive or destructive interference for a given product channel. The implications of the diffractive effects of SLMs depends on the nature of the target system as well as the geometry of the experiment. To quantify these effects, two parameters are considered for various mask configurations: (1) The spatial overlap integrals, within the focal volume, between different frequencies; (2) the relative strength of multiphoton transition probabilities, integrated across the focal volume. In the following configuration, we assume that relay optics have been used between the 4-f pulse shaper output and the experiment lens L3, in order to remove propagation effects.

Different frequencies will have different spatial structures as they evolve through the focus along the propagation direction. This will be important in experiments that rely on the nonlinear interaction of multiple frequencies. Figure 13 displays the electric field intensities of three different neighboring wavelengths $\lambda_i = 800$, 800.3, and 800.6 nm. Longer wavelength shifts display a similar variation. As a measure of the spatial variation of different colors through the focus, we use the normalized overlap integrals,

$$O_{\lambda_i\lambda_j} = \frac{\int I_{\lambda_i} I_{\lambda_j} dxdz}{\left(\int I^2_{\lambda_i} dxdz \int I^2_{\lambda_j} dxdz\right)^{1/2}}, \tag{26}$$

where $I_{\lambda_i}(x,z)$ represents the field intensity for a particular wavelength. The values of the overlap integrals $O_{\lambda_i\lambda_j}$ may vary considerably. A value of 1 indicates that two colors have complete overlap throughout the focal volume. Variations below 1 are significant because it implies that any multiphoton experiments that rely on the spatial overlap of several distinct colors will be affected by space-time coupling. Note, in Fig. 13, how the spatial structure varies rapidly with wavelength and that different frequencies do not overlap well. If the focal spot size at the SLM is decreased by a factor of 2 (from 38 μm to 19 μm), much of the structure still remains, since there will always be some frequencies that overlap pixel edges (Fig. 14)

The probability for a vertical n-photon transition having no intermediate resonances is given by the nth-order power spectrum, determined from conventional time-dependent perturbation theory [19]:

$$P_n(f_t,x,z) \propto \left| \int_{-\infty}^{\infty} e^n(t,x,z) e^{-2\pi i f_t} dt \right|^2 = |\mathcal{F}[E(t,x,z)]_{t\to nf_0 - f_t}|^2. \tag{27}$$

At first order, the transition is determined by the Fourier transform $P_1(f_t,x,z) \propto |e^t(f_t,x,z)|^2$ of the perturbation and the modulus removes any dependence on the phase of the electric field. At higher orders, however, the modulus is performed after the nth power is taken and the phase becomes the key element that influences the transition. All n-tuples of frequencies that add to the final frequency f_t are coherently summed and their spectral interference produces control.

In a system without space-time coupling, the transition probability (without intermediate resonances) is proportional to the peak intensity I at a point

$$P_n \propto I^n. \tag{28}$$

Therefore, the ratio between the nth- and mth-order multiphoton transitions

$$P_n / P_m^{n/m} \tag{29}$$

should be constant if only the peak intensity—and not the spectral content—at a spatial point is altered. In a space-time coupled system, however, the spectral content at each point changes throughout the focus. This result is illustrated in Fig.

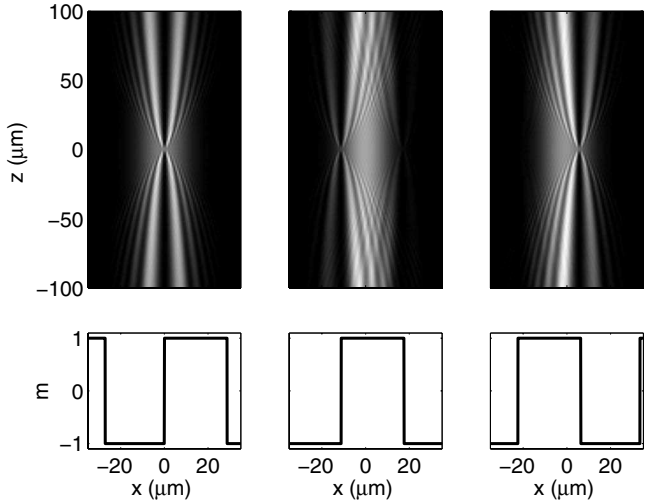

FIG. 13. Intensity plots at the focus, showing different spatial structures for different frequencies. From the left-hand side to the right-hand side the wavelengths are (1) 800 nm, (2) 800.3 nm, and (3) 800.6 nm. The normalized overlap integrals are $O_{1,2}=0.49$, $O_{1,3}=0.66$, and $O_{2,3}=0.60$, showing how diffractive effects can significantly modify the spatial overlap of different colors within the focus.

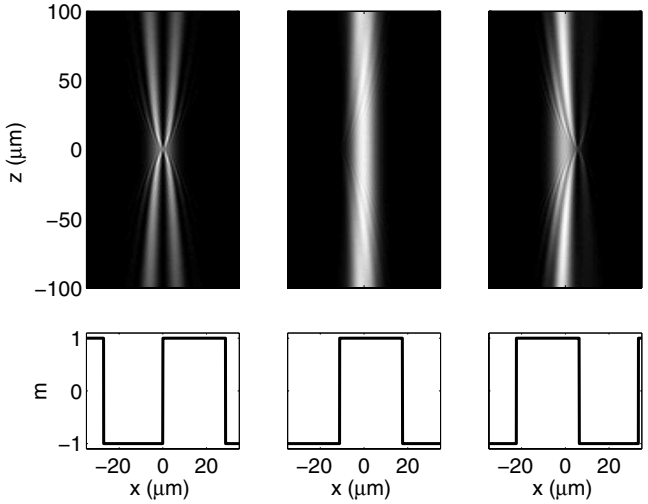

FIG. 14. Intensity plots at the focus, showing different spatial structures for different frequencies, but for a focal spot one-half the size of that in Fig. 13. From the left-hand side to the right-hand side the wavelengths are (1) 800 nm, (2) 800.3 nm, and (3) 800.6 nm. The normalized overlap integrals in this case are $O_{1,2}=0.59$, $O_{1,3}=0.54$, and $O_{2,3}=0.94$. Note that the reduced spot size at the SLM does not eliminate space-time coupling. (cf. Fig. 13)

15, where the ratios P_2/P_1^2 and $P_3/P_2^{3/2}$ are plotted, normalized with respect to the zero-space-time coupling result. It can be seen that diffractive effects significantly modify the spatial distribution of multiphoton transition probabilities beyond that expected from intensity considerations alone.

In order to quantify the effects of these deviations across the focal volume, the multiphoton branching ratios from (29) are normalized with respect to their non-space-time coupled values and their differences are integrated as

$$r_{nm} = \frac{\int |P_n/P_m^{n/m} - 1| dxdz}{\int dxdz}. \tag{30}$$

The results are displayed in Table II. In the absence of space-time coupling, these values would be zero. However, since the spectral content at each point is modified, the ratios from

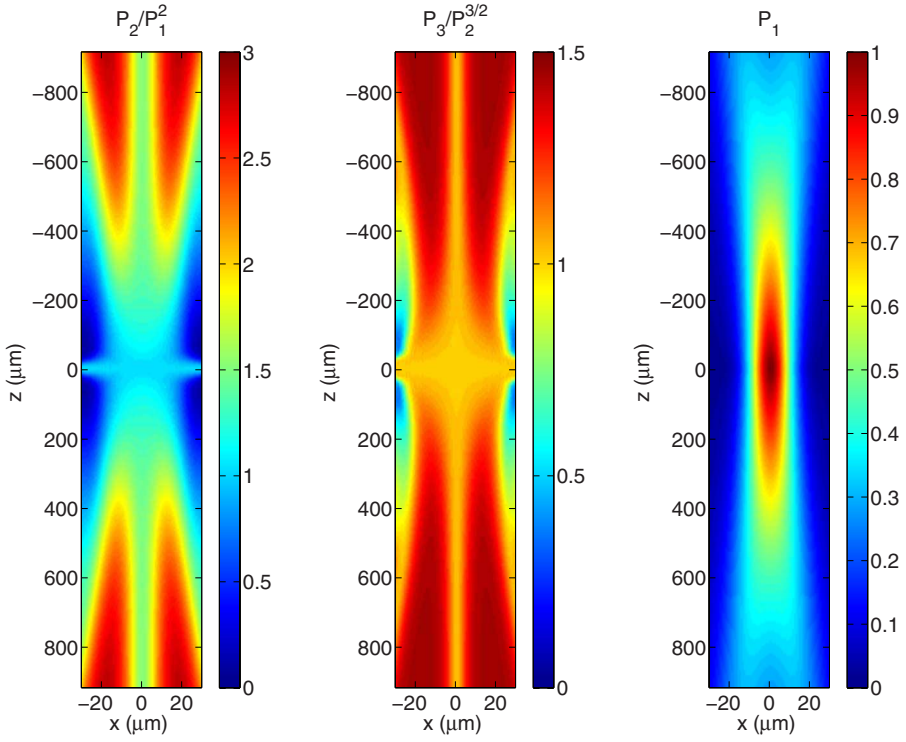

FIG. 15. (Color online) Normalized ratios of multiphoton transition probabilities plotted through the focus of a laser pulse from an SLM based 4-f pulse shaper with an alternating phase mask. As discussed in the text, these ratios are constructed to be intensity independent. Any deviation from 1 indicates that the spatial distribution of the spectral content has been altered by the space-time coupling. The rightmost figure displays the intensity of the beam, which has been included for comparison.

TABLE II. Focal volume integrated multiphoton transition probability ratio deviations (per unit area). In a system without space-time coupling, the ratios in (29) of multiphoton transition probabilities should be constant. However, the spectral change due to space-time coupling alters the ratios. Below, the deviation from 0 is due to the spatial change in spectrum caused by the space-time coupling. The ranges for the spatial integrals are $z=z_{\text{Rayleigh}}[-1,1]$, $x=\sqrt{2}\tau_x'[-1,1]$.

Mask	r_{21}	r_{32}
Transparent $m=\exp(i\pi[0,0,0,\ldots])$	0	0
Alternating phase $m=\exp(i\pi[1,0,1,0,\ldots])$	0.76	0.23
Small alternating phase $m=\exp(i\pi\sqrt{2}/3[1,-1,1,-1,\ldots])$	0.046	0.0036
Double alternating phase $m=\exp(i\pi[1,1,0,0,\ldots])$	0.89	0.24
Random phase $m=\exp(i2\pi[\text{rand}])$	0.44	0.12

(29) are not constant and their deviation from 1 can be considerable, as shown in Fig. 15. The transparent mask produces no space-time coupling and the deviation is zero. An alternating phase mask displays a considerable deviation. Doubling the period of the alternating mask does not reduce the deviation. That is, binning pixels together does not reduce the coupling. However, reducing the size of the pixel-to-pixel phase shift from π to $\sqrt{2}/3\approx 0.47$ [a fraction of constraint (25)] begins to satisfy (25), and therefore reduces space-time coupling. As an extreme case, a random phase mask was applied to each pixel [20]. The random mask is extremely efficient at reducing the higher order transition probabilities and shows considerable deviation from the non-space-time coupled case.

V. CONCLUSION

Spatial light modulators are an important tool for engineering optical wave forms and controlling quantum processes. Spatial modulation in a 4-f pulse shaper leads to both temporal and spatial changes in the propagated pulse. Due to space-time coupling, different spatial locations within the focus may experience different electric fields. The influence of space-time coupling on focused beams from SLM based 4-f pulse shapers can potentially have significant effects on experiments. Unfortunately, there are no simple rules for avoiding these effects and it is worthwhile to consider some limiting cases or to undertake simulations. The space-time coupling can usually be reduced by choosing parameters such that the spot size at the SLM for a single color is much smaller than the pixel size, i.e.,

$$\beta\frac{f_4\lambda_0}{\pi\tau_x} \ll W_p. \tag{31}$$

This constraint suggests as compact a pulse shaper as possible. Using smaller spot sizes at the SLM minimizes the multiplexing effects, depicted in Fig. 6, which occur when a spectral component straddles several pixels. However, even if this condition is met, there is still the possibility some of the optical frequencies of interest sit on pixel edges. For example, in a narrow resonance system, if the central frequency is dispersed about a pixel edge where neighboring pixels introduce different phases, there will be pixel-propagation diffractive effects and it may be useful to slightly translate the mask to center the optical frequency of interest to within a pixel. In general, the phase shift change per pixel should be kept sufficiently small via (25) in order to avoid the pixelation-propagation effects.

Strong space-time coupling can present challenges for the interpretation of quantum control measurements relying on SLM based 4-f pulse shaping. Because the applied field can vary across the focus, different target molecules may experience quite different electric fields. This means that the control mechanism will be averaged out or the relevant focal volume altered or shifted with respect to an independent probe laser. For the same reasons, inverting the results of control experiments in order to obtain information about atomic and molecular systems [21] will be more difficult if space-time coupling is significant.

An effective way to avoid space-time coupling is to use spatial filtering after the 4-f pulse shaper. The downside, of course, is extensive energy loss. For amplified laser systems, implementing the pulse shaper before the amplifier may reduce this coupling, since the amplifier modes themselves are usually much smaller than the seed laser mode and therefore can act as the spatial filter, in this case without any energy loss. Even in the absence of space-time coupling, the ratio of competing P^n to P^m processes will always scale as $I^{n-m}(x,z)$, so spatially selective probing within the focus (for example, by using a smaller probe laser focus) is always preferred.

APPENDIX A: FRESNEL PROPAGATION

Consider the analytic signal for a two-dimensional monochromatic plane wave traveling in the z direction,

$$e(x,z,t) = E(x,z)e^{i2\pi f_0 t}. \tag{A1}$$

The wave equation is given by [22]

$$[\nabla^2 + (2\pi f_0/c)^2]E(x,z) = 0. \tag{A2}$$

The envelope $E(x,z)$ may be written as a Fourier transform

$$E(x,z) = \int_{-\infty}^{\infty} E^{xz}(f_x,f_z)e^{2\pi i(f_x x+f_z z)}df_x df_z \tag{A3}$$

and inserted into the wave equation to produce the dispersion relationship

$$f_0^2/c^2 = f_x^2 + f_z^2 \tag{A4}$$

and specify

$$E^{xz}(f_x,f_z) = E^x(f_x;z_0)\,\delta\left(f_z \mp \frac{f_0}{c}\sqrt{1-c^2f_x^2/f_0^2}\right), \tag{A5}$$

where $E^x(f_x;z_0)$ is the one-dimensional Fourier transform at a specific transverse displacement z_0,

$$E^x(f_x;z_0) = \int_{-\infty}^{\infty} E(x,z_0)e^{2\pi i f_x x}dx. \tag{A6}$$

So that

$$E(x,z) = \int E^x(f_x;z_0)e^{\pm f_0/c\sqrt{1-c^2f_x^2/f_0^2}(z-z_0)+2\pi i f_x x}df_x. \tag{A7}$$

The sign of the root is a convention based on the direction of a traveling wave. Here the negative root is chosen. The generalization to three-dimensional space follows a similar path to that shown.

In the Fresnel limit, spatial frequencies are assumed to be small compared to the optical frequency, and the exponent is approximated as

$$f_z = \frac{f_0}{c}\sqrt{1-\frac{c^2f_x^2}{f_0^2}} \approx \frac{f_0}{c} - \frac{cf_x^2}{2f_0} \to -cf_x^2/2f_0. \tag{A8}$$

The term f_0/c, the net phase due to $\exp(2\pi i f_0 z/c)$, can be dropped unless phase comparisons are done between different paths. The evolution is then given by

$$E^x(f_x;z) = e^{-\pi i f_x^2(z-z_0)c/f_0}E^x(f_x;z_0) \tag{A9}$$

and the propagator is written as

$$U_{\text{Fresnel}}(f_x) = e^{-\pi i f_x^2(z-z_0)c/f_0}. \tag{A10}$$

This propagation can also be rewritten as a convolution, by using

$$\int a(y)b(x-y)dy = \int a^x(f_x)b^x(f_x)e^{-2\pi f_x x}df_x. \tag{A11}$$

Taking $a^x(f_x)=E^x(f_x;z_0)$, and $b^x(f_x)=e^{-\pi i f_x^2(z-z_0)c/f_0}$, the propagation can be written as

$$E(x,z) = \frac{1}{\sqrt{i\lambda_0(z-z_0)}}e^{i\pi f_0/c(z-z_0)x^2} \times \int E(x',z_0)e^{i\pi f_0/c(z-z_0)x'^2}e^{-2\pi i x x' f_0/(z-z_0)c}dx' \tag{A12}$$

which, owing to the fact that phases evolve slowly for large $z-z_0$, is useful for large distance numeric propagations.

For extreme variations in space—i.e., variations on the order of the wavelength—the Fresnel approximation is not valid as $cf_x \sim f_0$. Instead the complete exponent is used with the linear phase subtracted forming the complete scalar propagator

$$U(f_x) = e^{2\pi i\sqrt{(f_0/c)^2-(f_x)^2}(z-z_0)-2\pi i z f_0/c}. \tag{A13}$$

APPENDIX B: PROPAGATION THROUGH AN SLM BASED 4-*f* PULSE SHAPER

The effects of pulse propagation through a pulse shaper has been carefully detailed previously [14,15]. Here, the results are summarized and the focal field is derived. For the shaper in Fig. 1, there are 12 different steps from input beam to focal field, as enumerated below.

(1) An input beam $E(x,t)$ is dispersed by the input grating

$$E^t(x,f_t) \to \sqrt{\beta}E(\beta x, f_t - f_0)e^{2\pi i\gamma(f_t-f_0)}. \tag{B1}$$

(2) The beam is Fresnel propagated a distance f_4 via (A9).

(3) A thin lens introduces a quadratic spatial phase

$$E^t(x,f_t) \to E^t(x,f_t)U_{\text{lens}}(f_4), \tag{B2}$$

where the lens propagator is

$$U_{\text{lens}}(f_4) = e^{-\pi i f_0/cf_4x^2}. \tag{B3}$$

(4) The beam is Fresnel propagated a distance f_4 via (A9).

(5) The spatial mask is applied via multiplication

$$E^t(x,f_t) \to E^t(x,f_t)m(x). \tag{B4}$$

(6) The beam is Fresnel propagated a distance f_4 via (A9).

(7) A second, identical lens $U_{\text{lens}}(f_4)$ is applied.

(8) The beam is Fresnel propagated a distance f_4 via (A9).

(9) The second grating is applied in the inverted geometry:

$$E^t(x,f_t) \to \frac{1}{\sqrt{\beta}}E(-x/\beta, f_t - f_0)e^{2\pi i\gamma(f_t-f_0)}. \tag{B5}$$

(10) The beam is relayed a distance L via (A9) to the experimental lens.

(11) A thin lens of focal length f_L is applied using $U_{\text{lens}}(f_L)$.

(12) The beam is then Fresnel propagated to the focal plane.

The result is that the beam at the experimental focal plane is given by

$$E^t_{\text{focus}}(x,f_t) = E^{xt}_{\text{in}}\left(-\frac{x}{f_L\lambda_0},f_t\right)m\left(-\lambda_0 f_4\gamma f_t - \beta\frac{f_4}{f_L}x\right)e^{-i\pi L/\lambda_0 f_L^2x^2}. \tag{B6}$$

The argument of m indicates that the transverse position x at the focus is linearly related to the transverse position on the mask

$$x_{\text{mask}} = -\lambda_0 f_4\gamma f_t - \beta\frac{f_4}{f_L}x. \tag{B7}$$

At the focal plane the lines of constant displacement (or fixed pixel) are denoted by $f_t + x\frac{\beta}{\gamma\lambda_0 f_L} = \text{const}$. As the frequency is changed, so is the applicable pixel. Additionally, however, as the position changes so does the applicable pixel. It is important to note that (B6) relies on the Fresnel approximation (A9) and grating approximations [23]. The implications are that the above formalism does not include high spatial frequencies (e.g., the hard edges of the pixels) nor is it applicable for very large bandwidths or beam sizes.

APPENDIX C: NUMERICAL METHODS

The numeric propagation of pulses is efficiently achieved using the fast Fourier transform (FFT) and its inverse (IFFT), for transforming between coordinate space to frequency space. The propagation from longitudinal position z_0 to z can be done, using either (A9) or the convolution form from

(A12) and is simply a multiplication in frequency space, which can be written, respectively, as

$$E(x,z) = \mathcal{F}[e^{-i\pi f/cf_x^2(z-z_0)}\mathcal{F}^{-1}[E(x,z_0)]_{x\to f_x}]_{f_x\to x}, \quad \text{(C1)}$$

$$E(x,z) = \frac{1}{\sqrt{i\lambda(z-z_0)}}e^{i\pi f_0 x^2/c(z-z_0)} \times \mathcal{F}[E(x,z_0)e^{i\pi f_0 x^2/c(z-z_0)}]_{x\to xf_0/c(z-z_0)}. \quad \text{(C2)}$$

Care should be taken to assure that sampling is done correctly. Whereas complex data phase is only stored modulo 2π, the maximum variation $\delta_{\max}$ in the exponent phase of (C1) must be kept small (Nyquist theorem [24]),

$$\delta_{\max}(\pi f_0 f_x^2|z-z_0|/c) < \pi \to |z-z_0| < z_* \equiv n_x dx^2 c/f_0, \quad \text{(C3)}$$

where dx is the spatial grid step size, n_x is the number of spatial grid points, $\max(f_x)=1/2dx$, $df_x=1/n_x dx$. The inverse inequality $|z-z_0|>z_*$ holds for (C2), making it appropriate for large distances, although, this requires resampling of the spatial grid.

The number of temporal frequency points is reduced by sampling the pulse envelope instead of the instantaneous field $e(t)=E(t)e^{2\pi i f_0 t}$,

$$e(t) = \int e^t(f_t)e^{2\pi i f_t t}df_t = e^{2\pi i f_0 t}\int E^t(f_t)e^{2\pi i t}df_t. \quad \text{(C4)}$$

For products like (1) it is useful to note that multiplications in the frequency domain can be performed on the envelope transforms:

$$h(t) = \int e^t(f_t)g^t(f_t)e^{2\pi i f_t t}df_t = e^{2\pi i f_0 t}\int E^t(f_t)g^t(f_t+f_0)e^{2\pi i f_t t}df_t. \quad \text{(C5)}$$

[1] H. Kawashima, M. M. Wefers, and K. A. Nelson, Annu. Rev. Phys. Chem. **46**, 627 (1995).
[2] A. Assion, T. Baumert, M. Bergt, T. Brixner, B. Kiefer, V. Seyfried, M. Strehle, and G. Gerber, Science **282**, 919 (1998).
[3] R. J. Levis, G. M. Menkir, and H. Rabitz, Science **292**, 709 (2001).
[4] B. J. Pearson, J. L. White, T. C. Weinacht, and P. H. Bucksbaum, Phys. Rev. A **63**, 063412 (2001).
[5] Tobias Brixner and Gustav Gerber, ChemPhysChem **4**, 418 (2003).
[6] M. Dantus and V. V. Lozovoy, Chem. Rev. **104**, 1813 (2004).
[7] H. Rabitz, R. de Vivie-Riedle, M. Motzkus, and K. Kompa, Science **288**, 824 (2000).
[8] N. Dudovich, D. Oron, and Y. Silberberg, J. Chem. Phys. **118**, 9208 (2003).
[9] N. Dudovich, D. Oron, and Y. Silberberg, Nature (London) **418**, 512 (2002).
[10] F. Verluise, V. Laude, Z. Cheng, Ch. Spielmann, and P. Tournois, Opt. Lett. **25**, 575 (2000).
[11] A. M. Weiner, Rev. Sci. Instrum. **71**, 1929 (2000).
[12] T. Brixner and G. Gerber, Opt. Lett. **26**, 557 (2001).
[13] L. Polachek, D. Oron, and Y. Silberberg, Opt. Lett. **31**, 631 (2006).
[14] M. B. Danailov and I. P. Christov, J. Mod. Opt. **36**, 725 (1989).
[15] M. M. Wefers and K. A. Nelson, IEEE J. Quantum Electron. **32**, 161 (1996).
[16] T. Tanabe, H. Tanabe, Y. Teramura, and F. Kannari, J. Opt. Soc. Am. B **19**, 2795 (2002).
[17] Vincent Bagnoud and Jonathan D. Zuegel, Opt. Lett. **29**, 295 (2004).
[18] B. Wattellier, C. Sauteret, J.-C. Chanteloup, and A. Migus, Opt. Lett. **27**, 213 (2002).
[19] Doron Meshulach and Yaron Silberberg, Phys. Rev. A **60**, 1287 (1999).
[20] Makoto Matsumoto and Takuji Nishimura, ACM Trans. Model. Comput. Simul. **8**, 3 (1998). The random mask utilizes the first 128 numbers R_n from the Mersenne Twister algorithm (default seed 5489) to produce the mask $m_n=e^{2\pi i R_n}$.
[21] J. M. Geremia and Herschel Rabitz, Phys. Rev. Lett. **89**, 263902 (2002).
[22] J. W. Goodman, *Introduction to Fourier Optics*, 2nd ed. (McGraw-Hill, New York, 1996).
[23] O. E. Martinez, J. Opt. Soc. Am. B **3**, 929 (1986).
[24] William H. Press, Brian P. Flannery, Saul A. Teukolsky, and William T. Vetterling, *Numerical Recipes: The Art of Scientific Computing*, 2nd ed. (Cambridge University Press, New York, 1992).